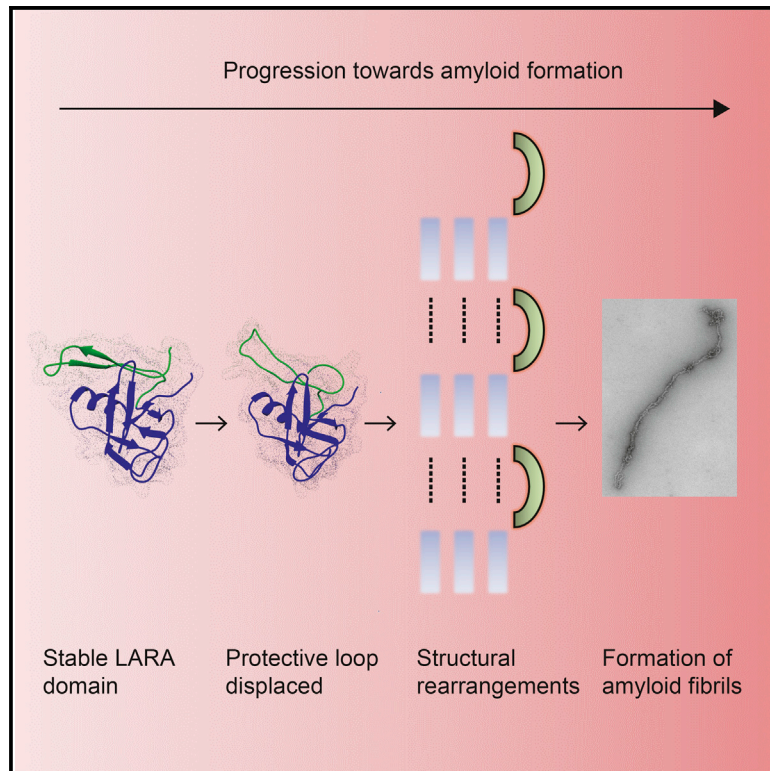# Mechanism of Amyloidogenesis of a Bacterial AAA+ Chaperone

## Graphical Abstract

## Authors

Sze Wah Samuel Chan, Jason Yau, Christopher Ing, ..., Régis Pomès, Simon Sharpe, Walid A. Houry

## Correspondence

ssharpe@sickkids.ca (S.S.),
walid.houry@utoronto.ca (W.A.H.)

## In Brief

Chan et al. make an unexpected observation that bacterial chaperone-like ATPase RavA and specifically the LARA domain within RavA readily form amyloids under acidic conditions at elevated temperatures. Experimental and theoretical studies revealed that the folded core of LARA is amyloidogenic and is protected by its N-terminal loop.

## Highlights

- Bacterial chaperone ATPase RavA was unexpectedly observed to form an amyloid state

- LARA domain of RavA drives amyloidogenesis at low pH and high temperatures

- LARA stability and dynamics were studied in detail using NMR and MD simulations

- Destabilization of the N-terminal loop of LARA initiates amyloid formation

CellPress

# Mechanism of Amyloidogenesis of a Bacterial AAA+ Chaperone

Sze Wah Samuel Chan,[1,5] Jason Yau,[1,2,5] Christopher Ing,[1,2] Kaiyin Liu,[1] Patrick Farber,[2] Amy Won,[3] Vaibhav Bhandari,[1] Nareg Kara-Yacoubian,[1] Thiago V. Seraphim,[1] Nilmadhab Chakrabarti,[2] Lewis E. Kay,[1,2,4] Christopher M. Yip,[1,3] Régis Pomès,[1,2] Simon Sharpe,[1,2,*] and Walid A. Houry[1,*]

[1]Department of Biochemistry, University of Toronto, 1 King's College Circle, Medical Sciences Building, Toronto, ON M5S 1A8, Canada
[2]Molecular Structure and Function Program, The Hospital for Sick Children, Toronto, ON M5G 1X8, Canada
[3]Institute of Biomaterials and Biomedical Engineering, University of Toronto, Toronto, ON M5S 3E1, Canada
[4]Department of Molecular Genetics, University of Toronto, Toronto, ON M5S 1A8, Canada
[5]Co-first author
*Correspondence: ssharpe@sickkids.ca (S.S.), walid.houry@utoronto.ca (W.A.H.)
http://dx.doi.org/10.1016/j.str.2016.05.002

## SUMMARY

**Amyloids are fibrillar protein superstructures that are commonly associated with diseases in humans and with physiological functions in various organisms. The precise mechanisms of amyloid formation remain to be elucidated. Surprisingly, we discovered that a bacterial _Escherichia coli_ chaperone-like ATPase, regulatory ATPase variant A (RavA), and specifically the LARA domain in RavA, forms amyloids under acidic conditions at elevated temperatures. RavA is involved in modulating the proper assembly of membrane respiratory complexes. LARA contains an N-terminal loop region followed by a β-sandwich-like folded core. Several approaches, including nuclear magnetic resonance spectroscopy and molecular dynamics simulations, were used to determine the mechanism by which LARA switches to an amyloid state. These studies revealed that the folded core of LARA is amyloidogenic and is protected by its N-terminal loop. At low pH and high temperatures, the interaction of the N-terminal loop with the folded core is disrupted, leading to amyloid formation.**

## INTRODUCTION

External influences such as thermal or acid stress can disrupt the native state of proteins, leading to exposure of aggregation-prone regions and giving rise to formation of non-native intermolecular β sheets. This can create a nucleus for protein aggregation, leading to the formation of amyloid fibrils (Eisenberg and Jucker, 2012). Amyloid fibrils are characterized by a cross β-sheet quaternary structure stacked perpendicular to the fibril axis (Moran and Zanni, 2014). This structure gives rise to protofilaments composed of core β-sheet strands strongly held together by a vast hydrogen-bonding network, which confers resistance to denaturation and proteolytic cleavage. Multiple protofilaments intertwine to form mature amyloid fibrils

containing a twisted spine arrangement having regular periodicity (Toyama and Weissman, 2011).

De novo kinetic formation of amyloids has typically been modeled by nucleation-dependent mechanisms comprising two distinct events: the formation of a thermodynamically disfavored nucleus followed by rapid elongation of thermodynamically favored fibrils (Knowles et al., 2014). However, key questions remain about the mechanisms that initiate the amyloid formation cascade. Considerable evidence in the field suggests that the process starts due to the exposure of amyloidogenic fragments that initiate assembly into large oligomers (Esteras-Chopo et al., 2005).

While many amyloids have been associated with diseases, bacterial amyloids have been shown to carry out diverse cellular roles. The most well-characterized functional bacterial amyloids are the extracellular curli fibers produced by many species of Enterobacteriaceae, and which are found to be involved in surface adhesion, cell aggregation, and biofilm formation (Barnhart and Chapman, 2006). The formation of amyloids has also been found to regulate protein toxicity. For example, microcin E492 from _Klebsiella pneumoniae_ forms an amyloid state that abolishes its toxicity (Marcoleta et al., 2013). Hence, knowledge of the form and function of bacterial amyloids is important for understanding bacterial physiology and pathogenicity.

We present the first report of a novel intracellular bacterial amyloid formed by the chaperone termed regulatory ATPase variant A (RavA). RavA is a hexameric gammaproteobacterial ATPase that belongs to the MoxR family of the ATPases associated with diverse cellular activities (AAA+) superfamily. Based on the X-ray crystal structure of RavA (El Bakkouri et al., 2010), a RavA protomer can be divided into three domains (Figures 1A and S1): an N-terminal AAA+ domain (containing the Walker A and B conserved nucleotide-binding motifs), a discontinuous triple-helical bundle, and a LARA (LdcI-associating domain of RavA) domain. The LARA domain is a protein-protein interaction domain required for association of RavA with an acid stress enzyme, the inducible lysine decarboxylase (LdcI) (El Bakkouri et al., 2010; Kanjee et al., 2011; Snider et al., 2006). Structurally, the LARA domain contains an N-terminal loop region (Q329–S360) and a folded core (T361–E440) that forms a β-sandwich-like fold (Figure 1A). The binding of RavA to LdcI
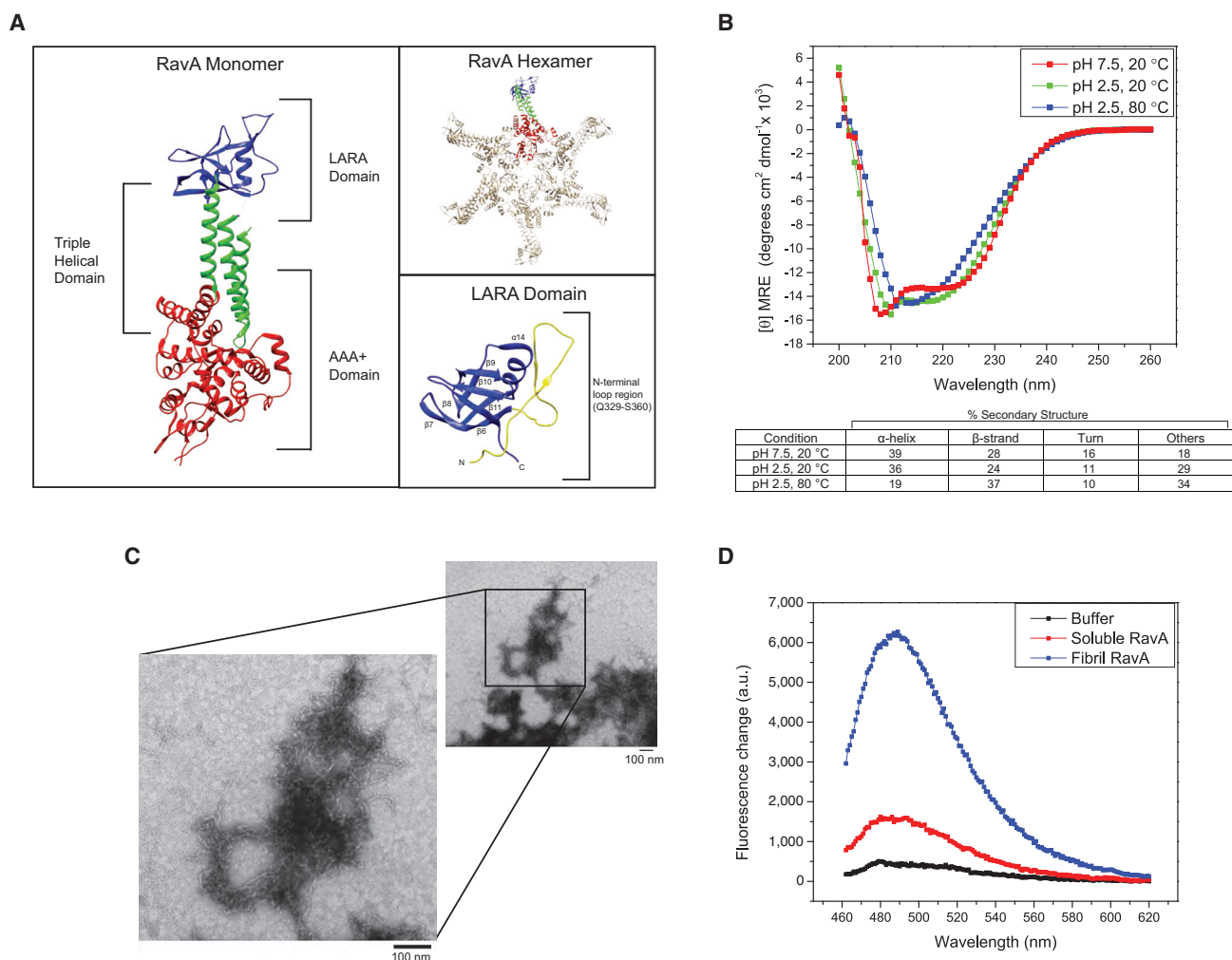
**A**



**B**



| | % Secondary Structure | | | |
|---|---|---|---|---|
| Condition | α-helix | β-strand | Turn | Others |
| pH 7.5, 20 °C | 39 | 28 | 16 | 18 |
| pH 2.5, 20 °C | 36 | 24 | 11 | 29 |
| pH 2.5, 80 °C | 19 | 37 | 10 | 34 |

**C**



**D**



**Figure 1. Formation of Amyloid Fibrils by RavA**

(A) Structure of Regulatory ATPase Variant (RavA) as described in El Bakkouri et al. (2010). Highlighted on the left are the three main domains of RavA: the AAA+ domain (red), the triple-helical bundle (green), and the LARA domain (blue). A RavA hexamer is shown in the top right box. A close-up view of the LARA domain is shown in the bottom-right box with the N-terminal loop in yellow. N refers to the N terminus and C refers to the C terminus. Secondary structure elements are labeled. See also Figure S1.

(B) CD spectra of RavA in pH 7.5 buffer at 20°C (red) and in pH 2.5 buffer at 20°C (green) and 80°C (blue). Predicted secondary structure content based on deconvolution using BeStSel (Micsonai et al., 2015) is shown underneath the figure.

(C) Negative-stain TEM images of RavA fibrils at 100,000× magnification.

(D) ThT fluorescence binding assay showing an emission wavelength scan from 462 to 620 nm for fibrillar RavA (blue), soluble RavA (red), and buffer (black).

results in the formation of a large cage-like structure that prevents the interaction of the alarmone, ppGpp, with LdcI (El Bakkouri et al., 2010; Kanjee et al., 2011). RavA has proposed chaperone activity involved in the maturation of the bacterial Nuo respiratory complex together with a cofactor protein termed ViaA (Wong et al., 2014). However, the functions and mechanisms of action of RavA, RavA-ViaA, and RavA-LdcI remain to be fully elucidated.

Full-length RavA was found to form an amyloid structure under conditions of low pH and elevated temperature, which is driven mainly by the LARA domain. Using various biochemical and biophysical approaches, we find that that the N-terminal loop region of the LARA domain has to rearrange to allow for amyloid formation by the β-rich core of the domain.

## RESULTS

### RavA Forms an Amyloid State at Low pH and High Temperature

Since RavA interacts with the acid stress protein LdcI (Snider et al., 2006), we became interested in studying the structural properties of RavA under acidic conditions. At pH 7.5 and 20°C, the circular dichroism (CD) spectrum of RavA was consistent with a predominately α-helical structure, with characteristic minima at 208 and 222 nm (Figure 1B). At pH 2.5 and 20°C, RavA displayed a similar CD profile to that observed at pH 7.5, but with slightly lower β-strand and turn content. However, at pH 2.5 and 80°C, the proportion of β-strand content increased to become the dominant secondary structure, concurrent with a decrease

in the α-helical signal (Figure 1B). Under these conditions, RavA formed aggregates that were visualized using transmission electron microscopy (TEM), revealing distinct fibrillar morphology (Figure 1C). The fibrils were non-rod like, instead having a curly appearance. Most of the fibrils appeared to bundle or twist together to form worm-like structures. These fibrils gave rise to an increase in thioflavin-T (ThT) fluorescence emission at 480 nm compared with soluble protein (Figure 1D), indicating the presence of extensive cross-β organization in the fibrils (Biancalana and Koide, 2010). Overall, these experiments suggest that acidic conditions and high temperatures induce a conformational change in RavA, resulting in the formation of a predominantly β-sheet fibrillar assembly.

## Formation of an Amyloid State by the LARA Domain

To determine which regions of RavA might be responsible for the formation of the amyloid state, we carried out in silico prediction of amyloidogenic sequences within RavA using MetAMYL (Emily et al., 2013), PASTA2.0 (Walsh et al., 2014), and AMYLPRED2 (Tsolis et al., 2013). Regions showing a consensus among two or three of the methods are indicated in Figure S1. Relatively few segments in the AAA+ domain and the triple-helical bundle had predicted amyloidogenic regions. Most of these predicted segments are in α helices, consistent with the suggestion that evolutionary pressure on protein sequence places amyloidogenic regions in α helices to prevent β-sheet aggregation (Monsellier and Chiti, 2007). On the other hand, the LARA domain exhibited many amyloidogenic regions that converged spatially around the β-sheet-rich core. Hence, we focused our subsequent studies on the isolated LARA domain.

As the LARA domain was heated at pH 6 from 20°C to 80°C, the protein structure was unfolded as shown by a loss of CD ellipticity at 217 nm (Figures 2A and S2A). Conversely, at pH 5 and lower, there was a gain in β-sheet structure as the temperature was increased (Figures 2A and S2A), with optimal conversion to a β-sheet-rich conformation at pH 4. Based on a sigmoidal fit of the melting curve (Figure 2A), the $T_m$ for the structural conversion at pH 4 was 42°C ± 0.1°C. We speculated that under these conditions, LARA was misfolding into an amyloid fibrillar state, which we name LARA$^{fib}$ (as opposed to the native, soluble LARA$^{sol}$). Based on CD fits for experiments at pH 4 and 20°C, there was an average of 25% ± 2% antiparallel β-sheet and 0% parallel β-sheet content predicted in the overall secondary structure for LARA$^{sol}$ (Figure S2A). For LARA$^{fib}$, the predicted secondary structure was 34% ± 5% antiparallel β-sheet and 11% ± 1% parallel β-sheet content at pH 4 and 50°C (Figure S2A).

The amyloid nature of the LARA$^{fib}$ state was confirmed by using ThT fluorescence. LARA$^{fib}$ formed by heating at pH 4 exhibited increased ThT fluorescence compared with buffer and LARA$^{sol}$ (Figure 2B). Based on Fourier transform infrared (FTIR) spectroscopy data, distinct structural differences between LARA$^{sol}$ and LARA$^{fib}$ were observed (Figure 2C). The amide I region (1,600–1,700 cm$^{-1}$) reflects the vibrational stretching of the amide backbone and is indicative of secondary structure (Sarroukh et al., 2013). Signal deconvolution using second derivative analysis was used to identify peaks that were subsequently fit to estimate secondary structure content. FTIR spectra of LARA$^{sol}$ show a β-sheet-dominant structure,

while deconvolution of the LARA$^{fib}$ FTIR spectra suggested a slight reduction in helix and coil content (Table S1). The shift in the β-sheet peaks to lower wavenumbers (for example, the dominant β-sheet peaks shifted from 1,640 cm$^{-1}$ in LARA$^{sol}$ to 1,619 cm$^{-1}$ in LARA$^{fib}$) is indicative of rearrangement of globular β sheets to extended β sheets, which is consistent with previous FTIR reports of amyloid fibrils (Sarroukh et al., 2013).

The LARA$^{sol}$ FTIR spectrum has a high-frequency band at 1,690 cm$^{-1}$ that indicates the presence of antiparallel β sheets. The FTIR spectrum of LARA$^{fib}$ exhibited a distinct increase in a similar region at 1,693 cm$^{-1}$, suggesting that LARA$^{fib}$ has higher antiparallel β-sheet content than LARA$^{sol}$. The β-sheet organizational index (intensity of the high-frequency component of antiparallel β sheets/intensity of the low frequency component of β sheets) is another measure used to compare antiparallel and parallel β-sheet content (Guo and Wang, 2012; Sarroukh et al., 2013; Zou et al., 2013). Antiparallel β-sheet content is correlated to the value of this index. For LARA$^{sol}$, the ratio is 0.22 compared with 0.39 for LARA$^{fib}$. The FTIR and CD data together suggest that LARA$^{fib}$ has increased antiparallel β-sheet content compared with LARA$^{sol}$.

When imaged using TEM (Figures 2D and S2B), LARA domain fibrils were observed to have the same twisted, curly fibril morphology observed for RavA (Figure 1C) and exhibited a similar worm-like clumping behavior. The morphology of these fibrils may indicate similarity between the assembly of LARA$^{fib}$ and fibrillar RavA. Preparation of LARA fibrils in different salt concentrations of 150 mM KCl, 50 mM KCl, and 10 mM KCl had no significant impact on the observed morphology of the fibrils (Figure S2B), indicating a lack of salt dependence within this salt concentration range.

The kinetics of LARA$^{fib}$ formation were monitored by ThT fluorescence at 33°C and pH 4 (Figure 2E). The $t_{0.5}$ for the fibrillization reaction was 373 ± 11 min obtained using a sigmoidal fit. Seeds created from sonicated fibrils decreased the $t_{0.5}$ to 277 ± 12 min with a corresponding 30-min decrease in the lag phase (Figure 2E and Table S2). With decreasing protein concentration, the lag phase and $t_{0.5}$ increased (Table S2), showing the expected dependence of nucleation events on protein concentration.

Subsequently, to identify the core region of LARA$^{fib}$, the broad-spectrum endopeptidase proteinase K was used to digest the fibrils. As shown in Figure S2C, SDS-PAGE analysis demonstrated that the majority of LARA$^{sol}$ was digested by 30–45 min. In contrast, several fragments of LARA$^{fib}$ remained protease resistant after 60 min of digestion. Digestion with trypsin followed by mass spectrometry was used to identify the components of the A (full length), B, and C bands observed for the proteinase K-treated fibril samples. Based on this analysis (Figure S2D and Table S3), we find that peptides corresponding to the N- and C-terminal ends of the protein are removed by proteinase K, while a fibril core corresponding to residues Q349–R423 was most resistant to proteolysis.

## Monitoring the Structural Changes Leading to LARA Amyloid Formation by NMR Spectroscopy

LARA$^{sol}$ backbone $^1$H, $^{15}$N, and $^{13}$C chemical shifts were assigned at pH 4 and 7°C, using a standard suite of triple-resonance experiments (Sattler et al., 1999) and were compared
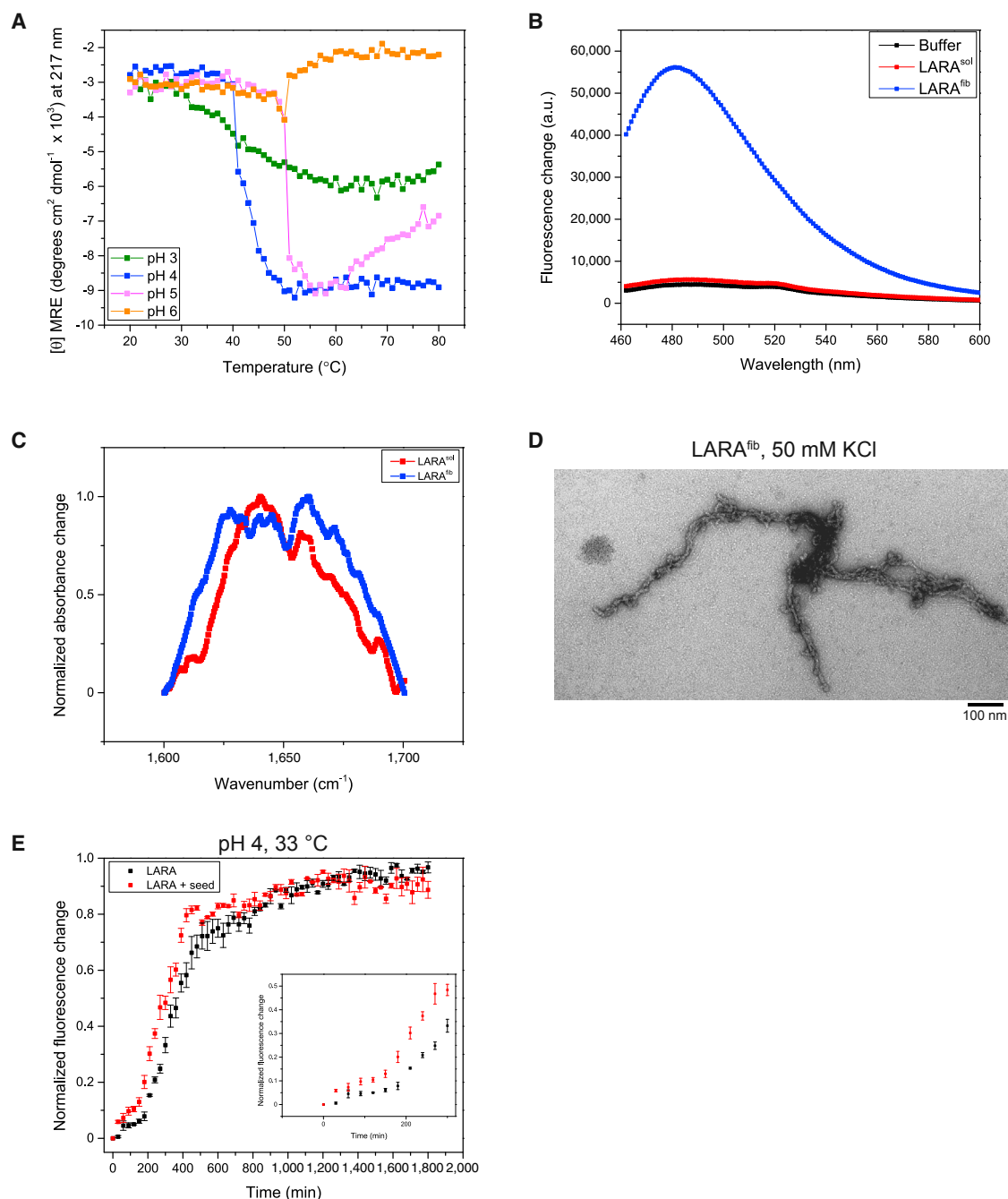
**Figure 2. Amyloid Fibrils Formed by the LARA Domain of RavA**

(A) The CD ellipticity of the LARA domain at 217 nm measured as a function of temperature (20°C–80°C) at pH 3 (green), pH 4 (blue), pH 5 (light magenta), and pH 6 (orange). See also Figure S2A.

(B) ThT fluorescence emission spectra after addition of buffer (black), LARA$^{sol}$ (red), and LARA$^{fib}$ (blue).

(C) Amide I region from the FTIR spectra of LARA$^{sol}$ (red) and LARA$^{fib}$ (blue). See also Table S1.

(D) TEM images of negatively stained LARA$^{fib}$ prepared in 50 mM KCl at 120,000× magnification. See also Figure S2B.

(E) ThT fluorescence emission at 480 nm monitored over time for LARA$^{sol}$ alone (black) and LARA$^{sol}$ + 2.5% (v/v) LARA$^{fib}$ seeds (red). The inset shows a close-up of the lag phase from 0 to 300 min. Errors bars represent the SEM for each data point (n = 3). See also Table S2.

with expected chemical shifts calculated from the crystal structure (El Bakkouri et al., 2010) (PDB: 3NBX) using SHIFTX2 (Han et al., 2011). A least-squared fit was performed comparing both Cα (R$^2$ = 0.943) and Cβ (R$^2$ = 0.991) resonances (Figure S3A). In addition, the secondary structure of LARA$^{sol}$ was predicted from the chemical-shift data using TALOS+ (Shen et al., 2009) and the Chemical Shift Index (Wishart and Sykes, 1994), the results of which were also compared with the

secondary structure elements identified in the crystal structure (Figure S3B). Both methods showed good agreement with the crystal structure (Figure S3B), indicating that the structure obtained at pH 6.5 using X-ray crystallography is similar to the LARA domain structure in solution at pH 4. The only structural differences suggested by our data were that the very N and C termini of the LARA domain were unstructured in solution, as expected for an isolated domain. Therefore, the X-ray structure was used as a model for the LARA domain when analyzing the experiments described below.

Heteronuclear single-quantum correlation (HSQC) spectra of LARA$^{sol}$ were recorded from 10°C to 30°C in a 5°C step gradient (Figure 3A), and then from 30°C to 40°C in a 2°C step gradient (data not shown). Fibrillization occurred between 30°C and 40°C and resulted in the loss of most resonances at 40°C due to significant line broadening, in agreement with the formation of large protein assemblies (Figure 3B). In these experiments, only 19 residues could be identified at 40°C (Table S4) that are primarily located in the N and C termini of the LARA domain, and which likely remain highly disordered and mobile in the fibril state. During the pre-unfolding transition, 99 residues could be tracked across the protein structure, providing probes for the conversion process from LARA$^{sol}$ to LARA$^{fib}$. During this transition the chemical shifts did not collapse into the random-coil region, suggesting that LARA$^{sol}$ does not globally unfold prior to oligomer formation.

The changes in chemical shift as a function of temperature were analyzed as shown in Figure 3C (examples are shown for boxed areas of Figure 3A) and are summarized in Figure 3D. Of particular interest, residues localized to the N-terminal loop (for example, Q350 and G343 in Figure 3C) exhibited significantly larger changes in chemical shift as a function of temperature when compared with residues in the folded core (Q418 and A386 in Figure 3C). All residues exhibited a linear change in $^1H$ and $^{15}N$ chemical shift with temperature, which has been shown to reflect the pre-unfolding transition (Farber et al., 2010). Overall trends from $^{15}N$ $\Delta\delta$ showed trends similar to those of $^1H$ $\Delta\delta$ (data not shown). The $^1H$ temperature coefficients corresponding to chemical-shift change per °C were then calculated (Cierpicki and Otlewski, 2001; Cordier and Grzesiek, 2002; Hong et al., 2013). These $^1H$ temperature coefficients are sensitive probes of hydrogen-bond stretching as well as hydrogen-bond interactions (Hong et al., 2013). Coefficients that are more negative than −4.5 ppb/°C correspond to residues forming hydrogen bonds with $H_2O$, while coefficients that are less negative than −4.5 ppb/°C correspond to sites forming protein-protein hydrogen bonds (Baxter and Williamson, 1997). Three regions of high thermal sensitivity stand out in this analysis (Figure 3D and Table S5): the N-terminal loop region, backside region of the LARA domain β-rich core (G395-S416), and the C terminus. The backside region exhibited a high temperature sensitivity, which may be due to exposure of these non-planar β sheets to solvent as a function of temperature. The C-terminal region is more disordered, and contains fewer hydrogen bonds, resulting in increased thermal instability. The N-terminal loop was generally more sensitive to temperature, with the heart-shaped part of the loop (V338–Y351) exhibiting the highest local thermal sensitivity, suggesting that this loop region undergoes a conformational change to begin the misfolding process.

Information on fast timescale protein dynamics was obtained from $^{15}N$ $R_2$, $R_1$ nuclear magnetic resonance (NMR) relaxation measurements and heteronuclear $^1H$,$^{15}N$ nuclear Overhauser effect measurements (pH 4, 24°C) carried out at 600 and 700 MHz. Lipari-Szabo model-free analysis (d'Auvergne and Gooley, 2008a, 2008b) was carried out on the LARA domain and the generalized order parameters ($S^2$) were determined (Figure S4). The protein can be divided into several segments based on the dynamics data. We observe a highly dynamic heart-shaped N-terminal loop with $S^2$ values lower than 0.75 consisting of residues V338–Y351. In addition, there is a rigid protein core of residues T361–A433, which mostly have $S^2$ values greater than 0.75. This analysis shows that the N-terminal loop (Q329–S360) may be amenable to structural rearrangements necessary for amyloid fibril formation.

### Probing Conformationally Excited States of the LARA Domain Induced by Low pH Using CPMG Relaxation Dispersion Experiments

To explore potential excursions from the ground state (LARA$^{sol}$) to sparsely populated, transiently formed conformers (referred to here as excited states), we performed $^{15}N$ Carr-Purcell-Meiboom-Gill relaxation dispersion (CPMG-RD) experiments (Korzhnev and Kay, 2008; Tollinger et al., 2001) under mildly destabilizing conditions (pH 4 and 24°C). These experiments permit the atomic resolution study of folding/unfolding events occurring in proteins on the millisecond exchange timescale by exploiting a series of spin-echo refocusing pulses at various frequencies (νCPMG) (Palmer et al., 2001). For such processes, the effect of exchange on the NMR signal intensities can be modulated as a function of νCPMG that is subsequently reflected in changes in observed transverse relaxation rates ($R_{2(eff)}$). Analysis of $R_{2(eff)}$ versus νCPMG provides quantitative information about the structural and kinetic properties of the excited state (Korzhnev and Kay, 2008).

Relaxation dispersion measurements of LARA$^{sol}$ were obtained using three NMR field strengths (600, 700, and 800 MHz) (Figures 4A–4D), and the dispersion profiles were globally fit to a single exchange process (reduced $\chi^2$ of 1.20, indicative of a reasonable fit), indicating local exchange of the native state with an excited state populated at 0.970% ± 0.003% and a $k_{ex}$ of 630 ± 31 s$^{-1}$. The residues that exhibited significant dispersion ($R_{ex} \geq 3$ Hz at 800 MHz) are labeled in Figure 4E, which shows that the majority of exchange with the excited state is localized primarily to the N-terminal loop region. The chemical-shift differences between the native and excited states (Δω) for residues in the N-terminal loop showed poor correlation with the chemical-shift differences between the native chemical shifts and those expected for random coil ($R^2$ of 0.14; Figure 4F). This indicates that the excited state of the N-terminal loop is not fully denatured but rather has a non-native but ordered structure.

### Molecular Dynamics Simulations of LARA Domain

To gain further insight into the conformational changes that take place leading to amyloid formation by the LARA domain, we carried out molecular dynamics (MD) simulations at pH 4 and 7, and 300 K (26.85°C). The root-mean-square fluctuation (RMSF) for each residue was tracked and averaged across simulations (Figure 5A). Within each condition, higher RMSF values
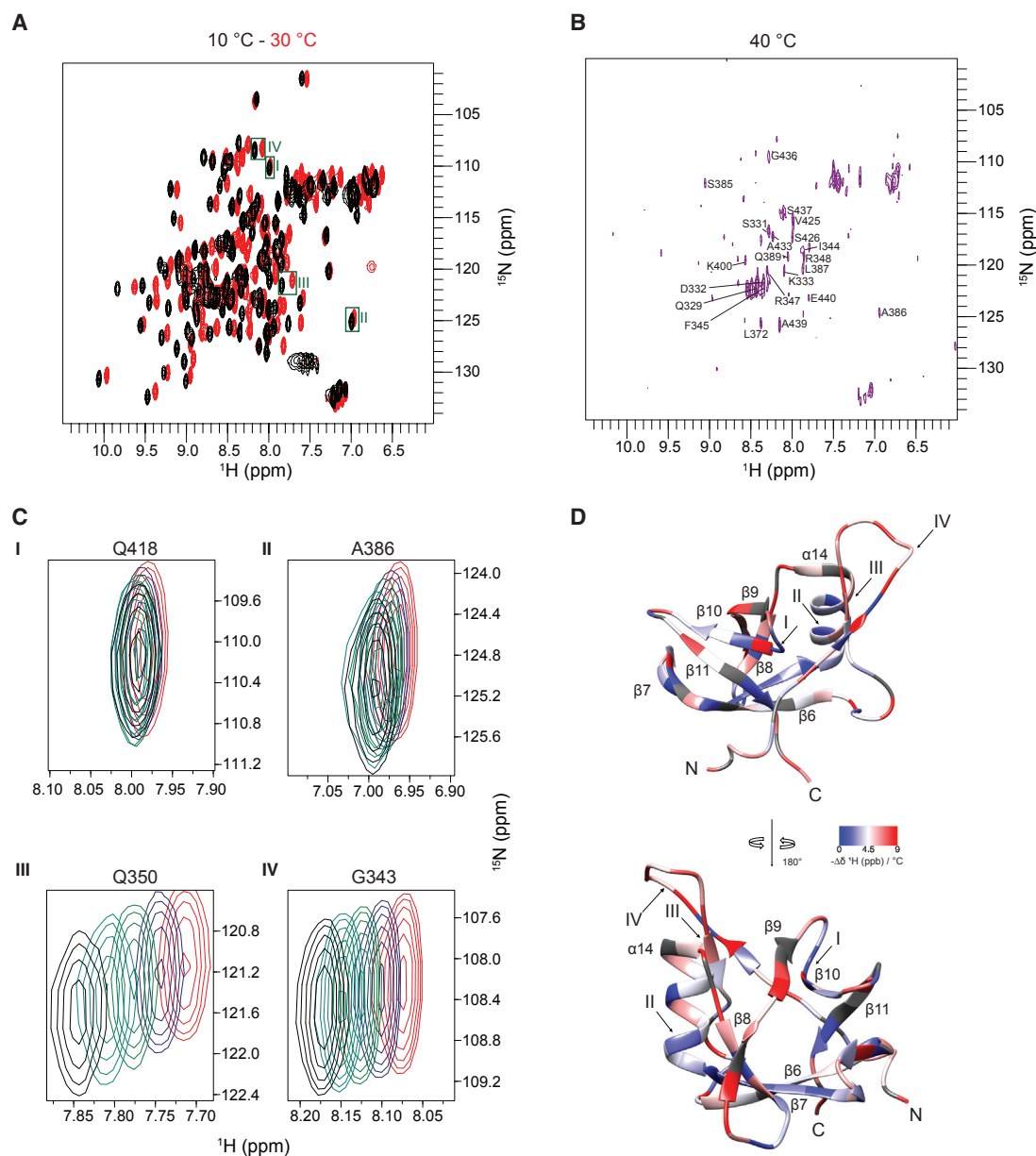
**Figure 3. ¹H,¹⁵N HSQC Spectra of the Soluble LARA Domain at Different Temperatures**

(A) ¹H,¹⁵N HSQC spectra of the LARA domain recorded at 10°C (black) and 30°C (red). Boxed peaks I and II show examples of residues with relatively low temperature coefficients, while III and IV are examples of residues having relatively high temperature coefficients.

(B) ¹H,¹⁵N HSQC spectrum of LARA^fib at 40°C. Backbone resonances that could be assigned at this temperature are labeled on the spectrum. See also Table S4.

(C) Examples of chemical-shift changes as a function of temperature for the residues identified in (A). Black is 10°C, turquoise is 15°C, green is 20°C, blue is 25°C, and red is 30°C.

(D) Temperature coefficients plotted on the structure of the protein with the locations of the residues highlighted in (A) and (C) indicated by roman numerals. Gray regions represent residues with unidentifiable coefficients due to inability to assign all the backbone resonances at all temperatures. The front (top) and back (bottom) faces of the LARA domain are shown, along with the corresponding color key (blue with low temperature coefficients and red with high temperature coefficients). See also Table S5.

were observed at the very N and C termini compared with the core, as expected. However, the heart-shaped region of the N-terminal loop (V338–Y351) exhibited significantly increased dynamics at pH 4 compared with pH 7 (Figure 5A). At pH 7, a major population was observed to form salt-bridge interactions (both direct hydrogen bonding and solvent mediated) between

the side chains of R340 and E413 (Figure 5B, top panel and Movie S1) or between R348 and E413 (Figure 5B, middle panel, and Movie S2). R340 and R348 were also observed to interchange salt-bridge interactions with E413 as shown in Movie S3, and were observed in some instances to interact simultaneously with E413 (Figure S5). Overall, these salt-bridge
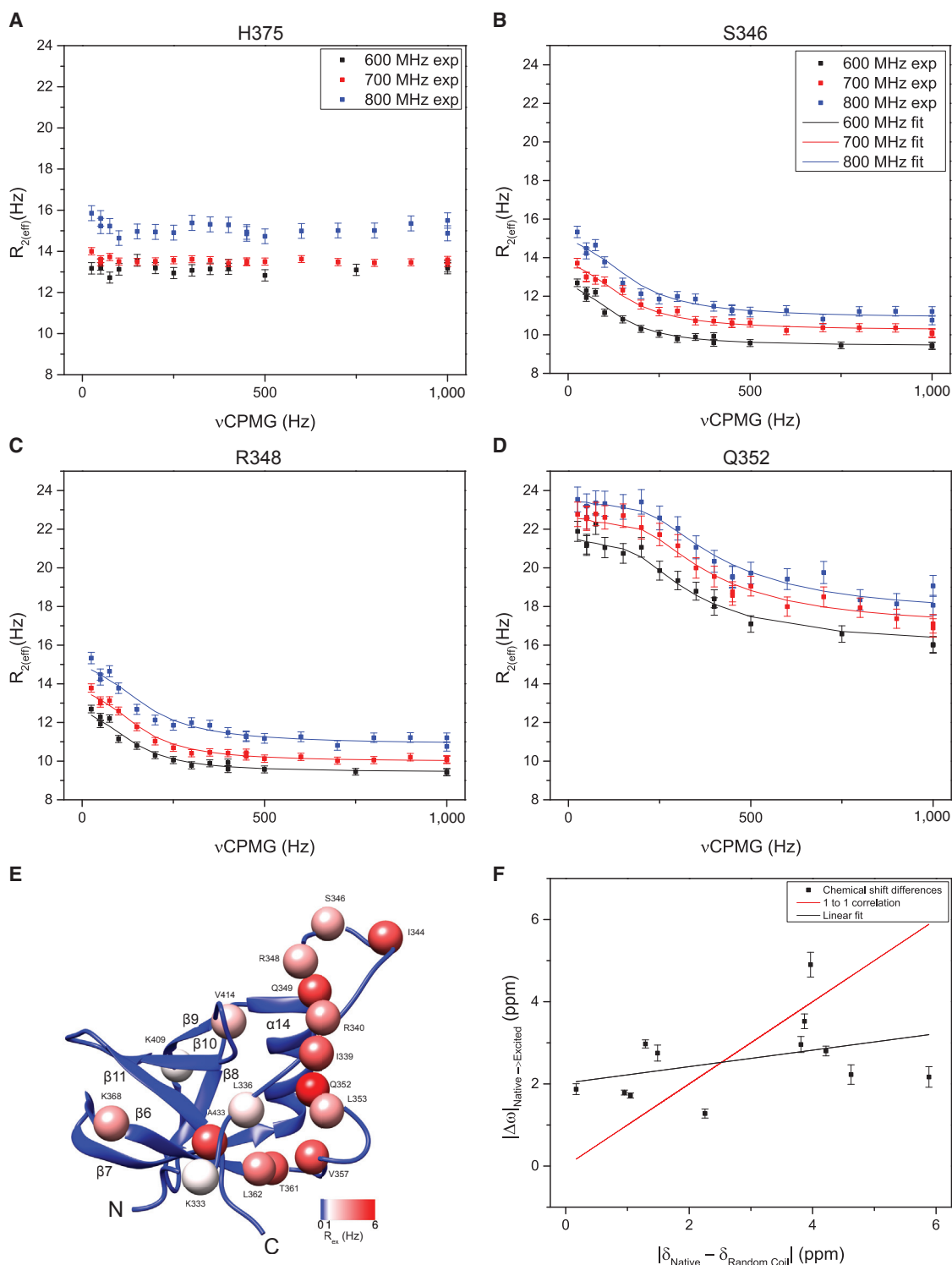
**Figure 4. CPMG Relaxation Dispersion Analysis of LARA<sup>sol</sup> at pH 4 and 24°C**

(A–D) $^{15}$N single-quantum $R_{2(eff)}$ as a function of CPMG frequency for several backbone amide resonances from the soluble LARA domain. CPMG-RD data were obtained at 600 MHz (black, lower), 700 MHz (red, middle), and 800 MHz (blue, top) $^1$H Larmor frequencies. (A) Shows a representative residue exhibiting no detectable relaxation dispersion, while (B–D) are examples of residues with significant relaxation dispersions due to chemical exchange. For each dataset showing significant relaxation dispersions due to chemical exchange (B–D), experimental data (exp) are shown along with global fitted values (fit) obtained using a two-state exchange between the ground and excited states. Errors bars shown are estimated errors in $R_{2(eff)}$ as described in the Supplemental Experimental Procedures. Legend inset in (B) also applies to (C) and (D).

*(legend continued on next page)*

**A**



**C**



**B**

pH 7, 300K,
490 ns (Run 3)
Video S1



pH 7, 300K,
778 ns (Run 2)
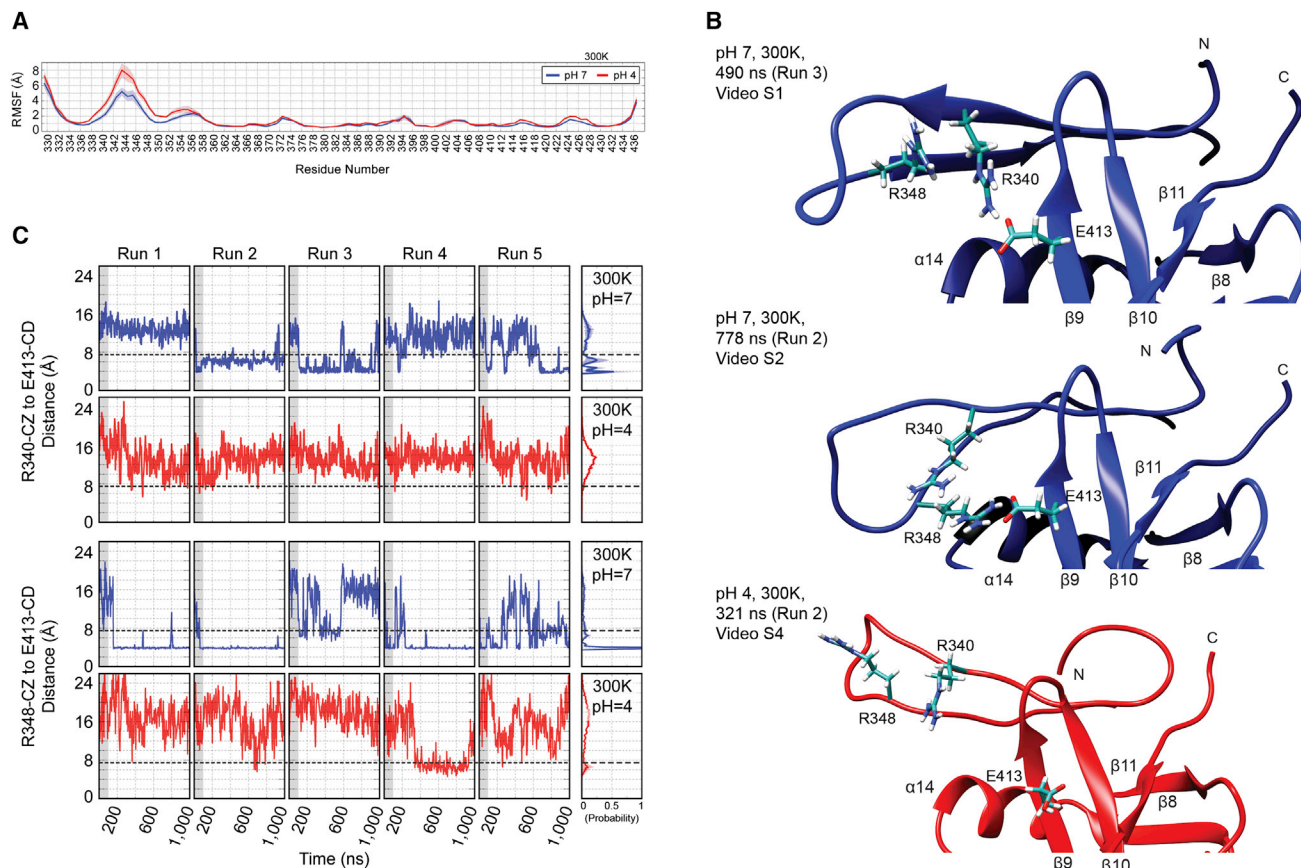Video S2



pH 4, 300K,
321 ns (Run 2)
Video S4



**Figure 5. Molecular Dynamics Simulations of the LARA Domain**

(A) Root-mean-square fluctuations (RMSF; Å) of residues of the LARA domain at pH 7 (blue) and pH 4 (red) at 300 K. Error bars are shaded and refer to the SEM (n = 5). See also Figure S5.

(B) The top panel shows an example of the salt bridge formed between R340 and E413 (at 490 ns in Movie S1, pH 7, run 3), while the middle panel shows the R348-E413 interaction (at 778 ns in Movie S2, pH 7, run 2). The bottom panel shows the loss of the salt bridges between R340-E413 and R348-E413 at pH 4 (at 321 ns in Movie S4, pH 4, run 2). See also Figure S5.

(C) Distances between the arginine $C\zeta$ and glutamic acid $C\delta$ for R340-E413 (top) and R348-E413 (bottom) through a series of 1,000-ns runs (runs 1–5) at pH 7 (blue) and pH 4 (red). The probability of distances across all runs are summed in the boxes to the right of run 5. The dashed line (7.5 Å) indicates the threshold of salt-bridge interactions, both solvent-mediated and direct contacts. The grayed-out regions (0–100 ns) were removed from the distance distribution calculation because the system may not be fully relaxed or equilibrated at these early time points.

interactions mediated loop closure over the β-rich core of the LARA domain. At pH 4, we observed disruption of these salt-bridge interactions due to protonation of E413 (Figure 5B, bottom panel, and Movie S4). Loss of these salt-bridge interactions at low pH likely gives rise to the increased dynamics of the heart-shaped region of the N-terminal loop in the simulations and as observed by NMR (Figures 3, 4, and S4). Note that the simulated protonation of the carboxylic acid moieties at low pH may lead to underestimation of the probability of salt-bridge formation compared with higher pH values.

If we define a Glu-Arg salt bridge as having a distance between the arginine $\zeta$ carbon and the glutamic acid $\delta$ carbon as <7.5 Å

(dotted line in Figure 5C), the probability of forming the salt bridge (both solvent-mediated and direct bonds) between R340 and E413 at pH 7 is 46% ± 19% (Figure 5C, blue curves at top), while the probability of the R348-E413 salt bridge is 68% ± 15% (Figure 5C, blue curves at bottom), giving a total salt-bridge formation probability of 86% ± 4% (R340 and/or R348 bonded to E413). The probability of both R340 and R348 forming simultaneous salt bridges with E413 is 28% ± 17%. None of these salt-bridge interactions were observed for an entire 1-μs trajectory; indeed, they were made and lost reversibly in four of the five simulations. In acidic conditions using the same criteria, the probability of forming similar salt bridges is 3% ± 8%

(E) $R_{ex}$ values (600 MHz) derived for each residue from the global fit analysis are plotted onto the LARA domain structure with each sphere representing one residue.

(F) Shown is a comparison of the chemical-shift difference between the native and excited states ($|\Delta\omega|$) of the LARA domain N-terminal loop residues and the magnitude of the chemical-shift difference between native (experimental) and random-coil (predicted) states (Wishart et al., 1995). Data were fit to a straight line (black line), while the correlation line expected for a fully unfolded excited state is shown as red.

and 10% ± 9% for E413-R340 and E413-R348, respectively (Figure 5C, red curves; total probability of 13% ± 9%). The formation of a combined salt bridge of R340 and R348 with E413 has a probability of 0.1% ± 0.1% under these conditions. Note that a minor metastable interaction between R348 side chain and G394 backbone carbonyl oxygen was observed in run 4 at pH 4, which led to a locally trapped minimum (Figures 5C and S5C).

## Mutations in the N-terminal Loop Region Enhance the Amyloid Formation Propensity of LARA

The HSQC and CPMG-RD experiments (Figures 3, 4, and S4) and MD results (Figure 5) strongly suggest that a conformational change in the N-terminal loop region is required for the formation of the amyloid state of the LARA domain. We speculated that the N-terminal loop must be displaced from the rest of the core LARA domain for amyloid formation to proceed. In this model, loop displacement exposes amyloidogenic regions, allowing for fibril formation through strand addition of LARA domain monomers to the exposed β-sheet edges in the core of the protein. To test this hypothesis, we generated a LARA domain construct, LARA(351–440), with a deletion of the N-terminal loop from residues 329–350, removing the Arg residues required for salt-bridge interactions with E413 (Figure 5).

CD spectra at 20°C and pH 4 of LARA(351–440) showed the presence of apparently increased β-sheet structure compared with the wild-type (WT) LARA domain at that same temperature and pH (Figure 6A). The altered shape of the CD spectrum might reflect a loss of random coil due to deletion of the N-terminal loop. Increasing the temperature at pH 4 resulted in even more β-sheet signal for LARA(351–440) (Figure 6A). LARA(351–440) also had a lower $T_m$ compared with WT (37.4°C ± 0.2°C versus 42.3°C ± 0.1°C) as monitored by CD at pH 4, suggesting a lower stability of the truncated protein. To further confirm our results, we measured the aggregation propensity of WT LARA and LARA(351–440) using static light scattering (SLS) at 266 nm. As shown in Figure 6B, LARA(351–440) aggregated at a lower temperature than WT LARA with a $T_{agg}$ (defined in Experimental Procedures) for LARA(351–440) of 30.5°C ± 0.5°C relative to 40.4°C ± 0.7°C for WT LARA. The higher starting SLS signal for LARA(351–440) may reflect a small population of pre-existing aggregates or fibrillar oligomers.

TEM analysis (Figure 6C) further confirmed the presence of worm-like fibrillar aggregates for LARA(351–440). Kinetic analysis of fibrillization showed that formation of LARA(351–440) amyloids was substantially faster than that of WT LARA, as monitored by ThT fluorescence at 33°C and pH 4 (Figure 6D and Table S2). This suggests that the barrier to amyloid formation is reduced for this mutant protein, consistent with our proposal that the N-terminal loop region plays a protective role in maintaining the native structure of the LARA domain.

FTIR analysis shows similarities between the estimated secondary structure of soluble LARA(351–440) and LARA[fib] (Figure 6E). In addition, the peaks corresponding to β-sheet amyloid peaks (1,620 cm$^{-1}$ region) align well between LARA(351–440)[sol] and LARA[fib] (Figure 6E). Along with the estimated secondary structure content (Table S1), these data suggest that LARA(351–440) retains a folded structure and that soluble LARA(351–440) has a fold similar to that of LARA[fib]. Furthermore, conversion of LARA(351–440)[sol] to

the amyloid state resulted in loss of α-helical content (Table S1). Moreover, LARA(351–440)[fib] has a smaller β-sheet peak at 1,634 cm$^{-1}$ and an increased amyloid β-sheet signal at 1,618 cm$^{-1}$ compared with LARA(351–440)[sol], suggesting extensive β-sheet rearrangements upon fibrillization by this truncation mutant.

Mutation of the positively charged R340, R347, and R348 to glutamate was carried out in the full-length LARA domain to further investigate the role of the salt-bridge interactions. The R347D mutation was made to prevent any compensatory salt-bridge interactions with E413. The triple mutant exhibited significantly faster amyloid formation kinetics relative to WT LARA (Figure 7A). The soluble and amyloid forms of the triple mutant and the WT LARA had generally similar FTIR spectra (Figure 7B, Table S1). Furthermore, TEM images of the LARA(R340D,R347D,R348D) amyloids showed fibrillar morphology similar to that of WT LARA[fib] (Figure 7C).

Finally, a thermal melt was conducted using nanoDSF (see Experimental Procedures) to measure the thermal stability of the different LARA domain mutants (Figure 7D). The ratio of integrated fluorescence emission intensity at 350 and 330 nm ($F_{350}/F_{330}$) was monitored as a function of temperature. The $T_m$ (defined in Experimental Procedures) was 42.6°C ± 0.04°C for WT LARA, 32.4°C ± 0.2°C for LARA(351–440), and 27.4°C ± 0.2°C for LARA(R340D,R347D,R348D). These trends show that both LARA mutants have lower thermal stability than WT LARA. The results of these experiments further support our proposal that salt bridges formed between R340/R348 and E413 stabilize LARA[sol] and reduce its rate of conversion to an amyloid state.

## DISCUSSION

While many amyloids are associated with neurodegenerative diseases, the amyloid states of proteins have also been found to perform functional roles in many different organisms (Eichner and Radford, 2011). Current structural data suggest that both functional and pathological amyloid fibrils share a similar cross-β architecture (Greenwald and Riek, 2010), yet the precise mechanisms by which proteins assemble into these ordered aggregates remain largely unknown (Goldschmidt et al., 2010). This study provides the first report of the formation of an amyloid state by the cytoplasmic E. coli AAA+ protein, RavA, and its LARA domain. Several bacterial cytoplasmic proteins are now known to form amyloid states including the GroES cochaperone from E. coli (Higurashi et al., 2005), the Rho termination factor from Clostridium botulinum (Pallares et al., 2015), as well as an artificial RepA-WH1 fusion construct used to model proteinopathy in bacteria (Torreira et al., 2015).

Both RavA and the LARA domain formed misfolded aggregates with typical amyloid characteristics, including a β-sheet-dominant secondary structure, binding to ThT, sigmoidal aggregation kinetics, protease resistance, and distinct fibrillar morphology (Eichner and Radford, 2011; Knowles et al., 2014; Nilsson, 2004). Conversion into the amyloid state by RavA was accompanied by a decrease in α-helical content, indicating a loss of structure in either the triple-helical bundle and/or the AAA+ module (Figure 1B). For the LARA domain, conversion to the amyloid state was similar and accompanied by formation of extended β-sheet structures, as
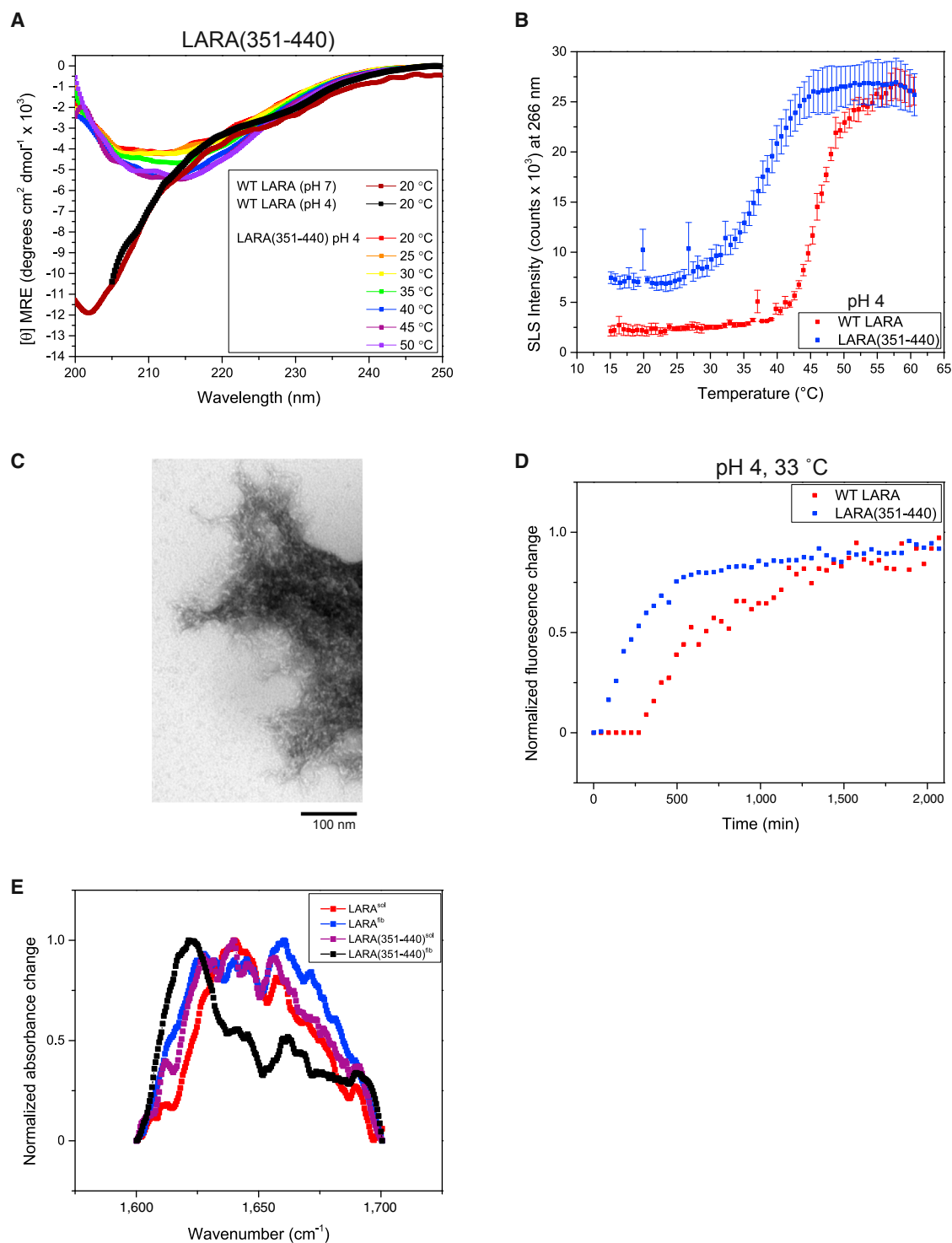
**Figure 6. Amyloid Formation by LARA(351–440)**

(A) CD spectra of LARA(351–440) recorded at pH 4 as a function of temperature. WT LARA[sol] (20°C) at pH 4 and pH 7 are shown as reference.

(B) Static light-scattering intensity at 266 nm for WT LARA (red) and the truncation mutant LARA(351–440) (blue) as a function of temperature. Error bars represent SEM (n = 3).

(C) TEM images of negatively stained LARA(351–440) fibrils viewed at 150,000× magnification.

(D) Representative curves of ThT fluorescence emission monitored over time for samples containing WT LARA (red) or LARA(351–440) (blue). Sample shown contained 15 μM protein at pH 4 and 33°C. See also Table S2.

(E) The Amide I region of FTIR spectra of LARA[sol] (red), LARA[fib] (blue), LARA(351–440)[sol] (purple), and LARA(351–440)[fib] (black). See also Table S1.
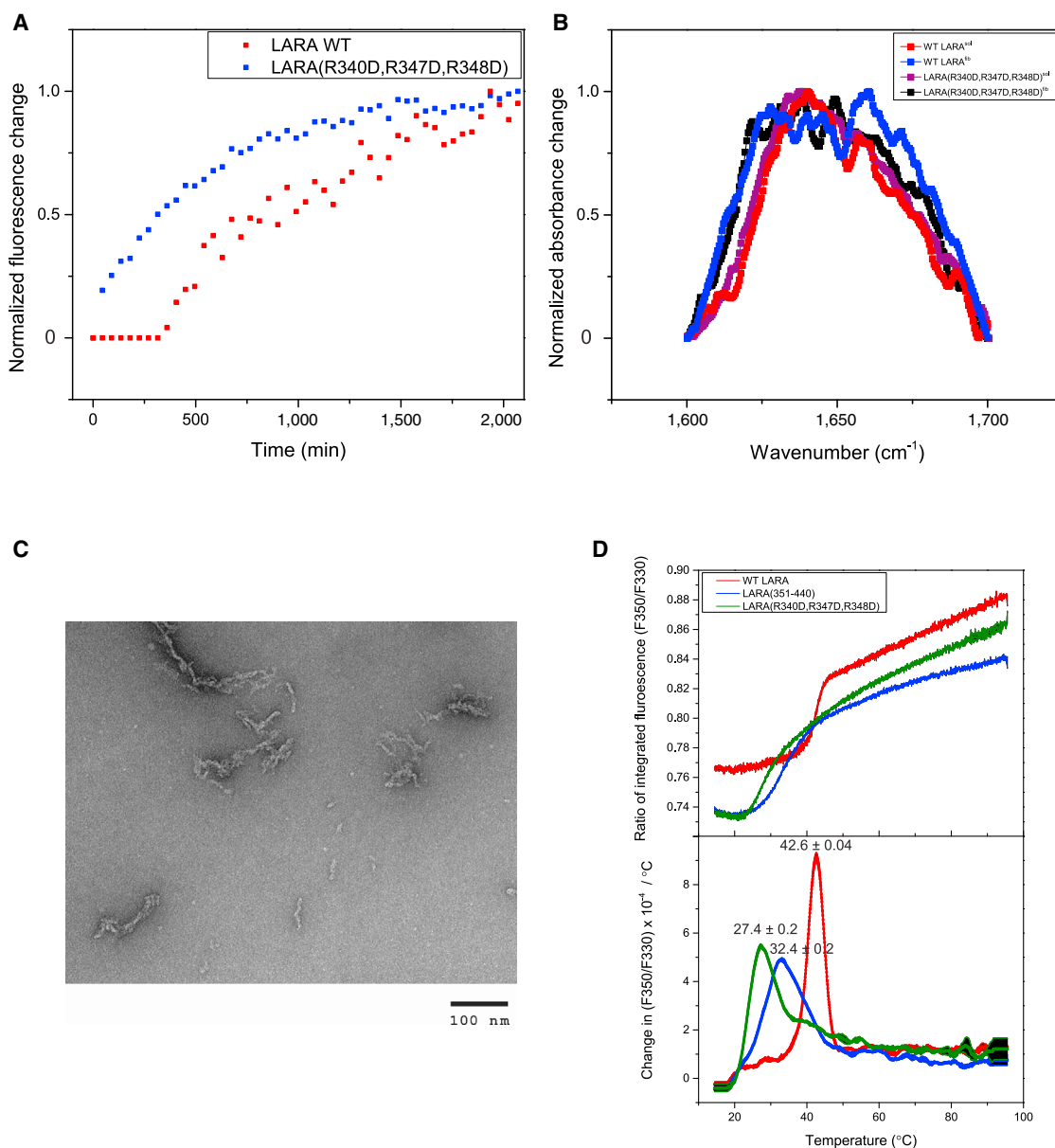
**Figure 7. Amyloid Formation by LARA(R340D,R347D,R348D)**

(A) Representative kinetic curves for amyloid formation monitored by ThT fluorescence emission are shown for LARA(R340D,R347D,R348D) in blue and for the WT LARA domain in red. Protein concentration was 10 μM at pH 4 and 33°C. See also Table S2.

(B) Amide I region from the FTIR spectra of LARA$^{sol}$ (red), LARA$^{fib}$ (blue), LARA(R340D,R347D,R348D)$^{sol}$ (purple), and LARA(R340D,R347D,R348D)$^{fib}$ (black). See also Table S1.

(C) TEM images of negatively stained LARA(R340D,R347D,R348D) fibrils at 120,000× magnification.

(D) nanoDSF analysis of a temperature melt of WT LARA (red), LARA(351–440) (blue), and LARA(R340D,R347D,R348D) (green). The black shading shows SEM (n = 3). The top panel is the $F_{350}/F_{330}$ ratio and the bottom panel is the first derivative of that curve with the $T_m$ for each LARA domain construct indicated.

suggested by the shift of β-sheet FTIR peaks to lower wavenumbers (Figure 2C).

Differences in fibrillar morphology have been suggested to result from different assembly pathways (Gosal et al., 2005; Miti et al., 2015). Variations in monomer conformation or in the intermolecular interfaces adopted during fibrillization may lead to the formation of different superstructures in mature amyloid fibrils. Both RavA and LARA fibrillar morphologies were twisted

and worm-like with extensive self-association between fibrils, potentially resulting from similar mechanisms of assembly. The ubiquitous nature of these twists and turns may be due to structural defects in the fibril backbone that are compensated for by the curvature. Similar worm-like fibrils have been observed for the mouse prion protein under low pH conditions (Jain and Udgaonkar, 2011), and for β-lactoglobulin (vandenAkker et al., 2011). In the latter case, worm-like fibrils were found to have
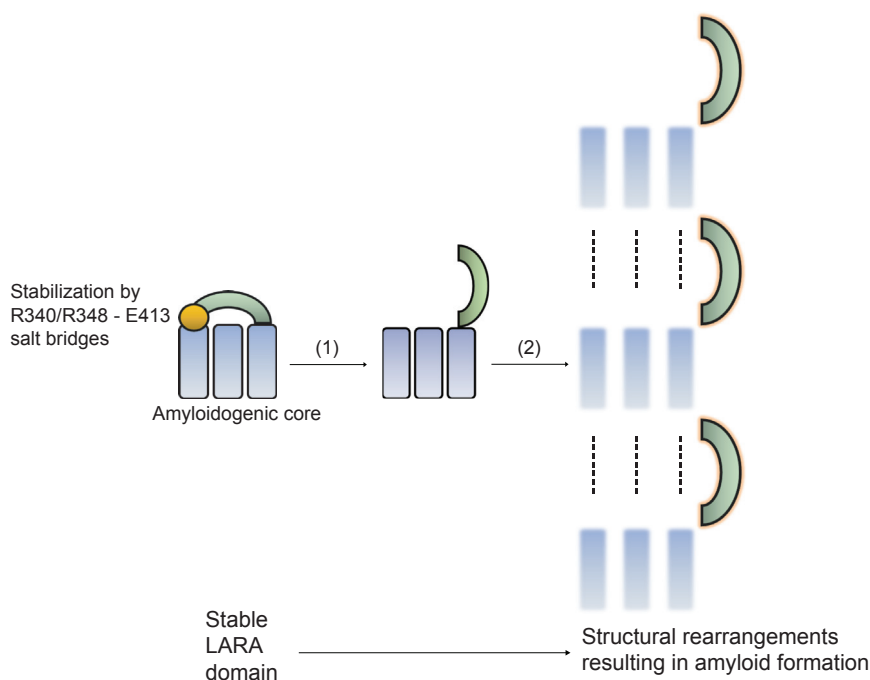
**Figure 8. Model of the Mechanism of Amyloid Formation by the LARA Domain**

On the left, the folded core of LARA (blue rectangles) is protected from aggregation by the N-terminal loop (green), which is held in position by the R340/R348-E413 salt-bridge interactions (orange circle). In step (1), acidic conditions disrupt the salt bridges, exposing the β-sheet edges. In step (2), partial destabilization of the core of the LARA domain and the N-terminal loop by increased temperature induces further structural rearrangements that promote non-native intermolecular contacts (dashed lines) and the formation of a nucleus that initiates the fibrillization process.

the surrounding core structures (α14, β6, and β11) are also relatively temperature insensitive (Figure 3 and Table S5). CPMG-RD analysis (Figure 4) showed that these core structural elements display almost undetectable relaxation dispersions under the mild conditions that destabilized the N-terminal loop. Based on multiple amyloid prediction algorithms (Figure S1), this β-sheet-rich core of the LARA domain, especially β6 and β7, contains highly amyloidogenic segments. Furthermore, the LARA domain construct lacking the N-terminal loop rapidly forms amyloid fibrils and displays a secondary structure similar to that of LARA$^{fib}$ (Figure 6). Combined with the similarity in the proteolysis pattern between LARA$^{sol}$ and LARA$^{fib}$ (Figure S2C), the lack of a detectable global unfolding event from solution NMR (Figure 3A), and similarity in flexible residues after oligomer formation (Figure 3B), we propose that the core of the LARA amyloid fibrils retains a structure close to that of LARA$^{sol}$. The combination of low pH and high temperature is sufficient to destabilize the N-terminal loop, expose amyloidogenic regions, and slightly destabilize the packing of the β-sheet region to allow formation of a native-like nucleus that initiates amyloid formation (Figure 8).

The LARA domain is required for the association of RavA with LdcI to form the RavA-LdcI 3 MDa cage-like complex (Malet et al., 2014; Snider et al., 2006), in which the N-terminal loop of the LARA domain forms specific intermolecular contacts essential for RavA-LdcI interactions (Malet et al., 2014) (Figure S6). It is interesting to note that LdcI is induced at low pH and forms the RavA-LdcI cage structure under these acidic conditions. While previous experiments suggest that the RavA, ViaA, and LdcI might be required to modulate the assembly of respiratory complexes in *E. coli* (Erhardt et al., 2012; Wong et al., 2014), another function of the cage structure might be to stabilize the LARA domain of RavA and prevent the formation of RavA amyloids when the bacteria encounter low-pH and high-temperature conditions.

significantly lower β-sheet content relative to straight fibrils, suggesting differences in internal structure and assembly (vandenAkker et al., 2011). A similar worm-like fibril morphology has been reported for amyloid fibrils formed by an SH3 domain mutant which mimics a folding intermediate (Neudecker et al., 2012). In this SH3 mutant, deletion of a protective β strand allowed exposure of aggregation-prone regions and promoted amyloid formation in a manner similar to protein misfolding. These observations suggest that exposure of the amyloidogenic-prone regions in the LARA domain could result in rapid nucleation events that parallel the aggregation process of a destabilized protein misfolding intermediate.

From the NMR thermal melts (Figure 3), CPMG-RD analysis (Figure 4), and MD data (Figure 5), the N-terminal loop region of the LARA domain is implicated in the amyloid formation process. MD showed a distinct mechanism for stabilization of the native fold through salt-bridge interactions of R340 and R348 with E413 that bring the heart-shaped loop region over the exposed β strands. This loop interaction is disrupted under conditions of low pH due to increased protonation of glutamic acid side chains. Deletion of the loop region, or mutagenesis of salt-bridge-forming residues, resulted in a significantly increased rate of in vitro amyloid fibril formation (Figures 6B, 6D, and 7A). Hence, we propose that the N-terminal loop inhibits amyloid formation by the LARA domain of RavA, and, therefore, plays a protective role in stabilizing the soluble native form of the protein. Since this region of the protein is relatively flexible under conditions of low pH and elevated temperature, the loop is able to access non-native conformations and lower the barrier to amyloid formation.

Another interesting observation is that residues of the β7 strand (M375–E383) have the smallest, in absolute value, $^{1}$H temperature coefficients (Δδ/°C of −2.9 ppb, Table S5 and Figure 3D). This β strand is located within the core of the protein;

In conclusion, our study describes a new amyloid-forming protein and adds to the current list of amyloids formed by bacterial proteins. It provides critical insights into the mechanism of amyloidogenesis by the LARA domain of RavA. The physiological roles played by the RavA amyloids in the context of bacterial viability and pathogenesis remain to be elucidated.

However, the pH sensitivity of amyloid formation by a protein involved in the cellular acid stress response pathway raises intriguing functional possibilities for the role of such amyloids in pathogenesis.

## EXPERIMENTAL PROCEDURES

Protein expression and purification and all biophysical and biochemical experiments are further described in detail in Supplemental Experimental Procedures.

### Protein Purification
Expression and purification of proteins were conducted according to standard protocols described previously (El Bakkouri et al., 2010). RavA and LARA were purified using nickel-nitrilotriacetic acid-agarose chromatography. Elutions were subsequently further purified using cation-exchange and flash-frozen with liquid nitrogen. For isotopic labeling, cells were induced with 0.5 mM iso-propyl β-D-1-thiogalactopyranoside for 4 hr at 30°C in M9 Minimal Medium supplemented with 1 g/l $^{15}NH_4Cl$ and 2 g/l $[^{13}C]$glucose.

### Amyloid Fibril Preparation
LARA was dialyzed into pH 4 buffer and RavA was buffer exchanged into pH 2.5 buffer. RavA and LARA were then converted into amyloids by heating from 20°C to 80°C at 1°C/min.

### ThT Fluorescence Assay
ThT fluorescence change was measured with excitation set at 442 nm and emission set at 480 nm for kinetic experiments at a constant temperature of 33°C to initiate fibrillization. Fluorescence emission spectra were scanned from 462 to 600 nm to assess ThT binding. A concentration of 20 μM ThT was typically used in these experiments.

### Transmission Electron Microscopy
RavA or LARA domain fibrils were prepared using general procedures outlined in Walsh et al. (2009). Samples were adsorbed onto continuous carbon films from copper rhodium grids (Electron Microscopy Sciences) and glow-discharged for 15 s at 30 mA negative discharge. TEM images were obtained using a JEOL 1011 microscope operating at 80 keV.

### CD Spectroscopy
The secondary structure of full-length RavA and the isolated LARA domain were analyzed using a JASCO J-810 spectropolarimeter with a 1.0-mm path-length quartz cuvette. The temperature was raised at a rate of 1°C/min and spectra were typically collected at every 5°C (200–260 nm range) with a scanning speed of 50 nm/min.

### Attenuated Total Reflectance (ATR)-FTIR Spectroscopy
A Nicolet Nexus 6700 FTIR spectrometer (Thermo Fisher Scientific) coupled with a Smart Orbit ATR unit was used to measure the infrared spectra. For each spectrum, 512 scans were collected with a resolution of 1 cm$^{-1}$ over a scan range of 4,000–525 cm$^{-1}$ using Ominic software. In the text, ATR-FTIR is referred to as FTIR.

### NMR Spectroscopy
Bruker Avance III 600-MHz and 700-MHz spectrometers were used to collect data for all experiments using a 5-mm TXI triple-resonance probe equipped with z-gradient pulse-field gradient capabilities. Relaxation dispersion experiments were also recorded at 800 MHz on a Varian Unity Inova four-channel spectrometer using a 5-mm, triple-resonance, three-axis pulse-field gradient probe. Thermal melt of soluble $^{13}C$, $^{15}N$-labeled LARA was monitored using 2D $^1H$,$^{15}N$ HSQC spectra. Data were acquired every 5°C for 7 min between 10°C and 30°C and every 2°C for 5 min between 30°C and 40°C. 4,4-dimethyl-4-silapentane-1-sulfonic acid was used as an external reference at each temperature.

$^{15}N$ CPMG relaxation dispersion profiles of $^{15}N$-labeled LARA domain were measured with a $^1H$-decoupled $^{15}N$ CPMG-HSQC pulse sequence (Tollinger et al., 2001) at 24°C. CPMG refocusing pulse frequencies (νCPMG) between 0 and 1,000 Hz were employed over a constant CPMG time-relaxation interval of 40 ms. Relaxation dispersion profiles of LARA$^{sol}$ were recorded at three fields (600, 700, and 800 MHz $^1H$ frequency).

### MD Simulations
The LARA domain of RavA was used for MD simulations based on the PDB: 3NBX crystal structure. The protein was solvated in a rectangular cell for pH 7 simulations and in a rhombic dodecahedron cell for pH 4 simulations. Na$^+$ and Cl$^-$ ions were added to each simulation box to obtain a net charge of zero and approximately 150 mM excess salt. All simulations were performed using GROMACS (Pronk et al., 2013). The optimized potentials for liquid simulations all-atom force field (Jorgensen et al., 1996; Kaminski et al., 2001) were used to model the protein and ions. The transferable intermolecular potential 3-point model (Jorgensen et al., 1983) was used for water molecules.

## ACCESSION NUMBERS

Resonance assignments have been deposited in the Biological Magnetic Resonance Bank database under accession number BMRB: 26735.

## SUPPLEMENTAL INFORMATION

Supplemental Information includes Supplemental Experimental Procedures, six figures, five tables, and four movies and can be found with this article online at http://dx.doi.org/10.1016/j.str.2016.05.002.

## AUTHOR CONTRIBUTIONS

S.W.S.C., K.L., S.S., and W.A.H. were involved in the study conception and experimental design. S.W.S.C., K.L., V.B., T.V.S., and N.K.Y. prepared samples and conducted the biophysical and biochemical experiments. J.Y. was responsible for the NMR spectroscopy data acquisition and along with P.F. and L.E.K. carried out the NMR data analysis. C.I., N.C., and R.P. were responsible for collecting and analyzing the MD data. A.W. was responsible for analyzing and collecting the ATR-FTIR data. C.M.Y., R.P., S.S., and W.A.H. helped provide experimental input. S.W.S.C., S.S., and W.A.H. were primarily responsible for drafting the manuscript.

## ACKNOWLEDGEMENTS

## REFERENCES

Barnhart, M.M., and Chapman, M.R. (2006). Curli biogenesis and function. Annu. Rev. Microbiol. 60, 131–147.

Baxter, N.J., and Williamson, M.P. (1997). Temperature dependence of $^1H$ chemical shifts in proteins. J. Biomol. NMR 9, 359–369.

Biancalana, M., and Koide, S. (2010). Molecular mechanism of thioflavin-T binding to amyloid fibrils. Biochim. Biophys. Acta 1804, 1405–1412.

Cierpicki, T., and Otlewski, J. (2001). Amide proton temperature coefficients as hydrogen bond indicators in proteins. J. Biomol. NMR 21, 249–261.

Cordier, F., and Grzesiek, S. (2002). Temperature-dependence of protein hydrogen bond properties as studied by high-resolution NMR. J. Mol. Biol. 317, 739–752.

d'Auvergne, E.J., and Gooley, P.R. (2008a). Optimisation of NMR dynamic models I. Minimisation algorithms and their performance within the model-free and Brownian rotational diffusion spaces. J. Biomol. NMR 40, 107–119.

d'Auvergne, E.J., and Gooley, P.R. (2008b). Optimisation of NMR dynamic models II. A new methodology for the dual optimisation of the model-free parameters and the Brownian rotational diffusion tensor. J. Biomol. NMR 40, 121–133.

Eichner, T., and Radford, S.E. (2011). A diversity of assembly mechanisms of a generic amyloid fold. Mol. Cell 43, 8–18.

Eisenberg, D., and Jucker, M. (2012). The amyloid state of proteins in human diseases. Cell 148, 1188–1203.

El Bakkouri, M., Gutsche, I., Kanjee, U., Zhao, B., Yu, M., Goret, G., Schoehn, G., Burmeister, W.P., and Houry, W.A. (2010). Structure of RavA MoxR AAA+ protein reveals the design principles of a molecular cage modulating the inducible lysine decarboxylase activity. Proc. Natl. Acad. Sci. USA 107, 22499–22504.

Emily, M., Talvas, A., and Delamarche, C. (2013). MetAmyl: a META-predictor for AMYLoid proteins. PLoS One 8, e79722.

Erhardt, H., Steimle, S., Muders, V., Pohl, T., Walter, J., and Friedrich, T. (2012). Disruption of individual nuo-genes leads to the formation of partially assembled NADH:ubiquinone oxidoreductase (complex I) in Escherichia coli. Biochim. Biophys. Acta 1817, 863–871.

Esteras-Chopo, A., Serrano, L., and Lopez de la Paz, M. (2005). The amyloid stretch hypothesis: recruiting proteins toward the dark side. Proc. Natl. Acad. Sci. USA 102, 16672–16677.

Farber, P., Darmawan, H., Sprules, T., and Mittermaier, A. (2010). Analyzing protein folding cooperativity by differential scanning calorimetry and NMR spectroscopy. J. Am. Chem. Soc. 132, 6214–6222.

Goldschmidt, L., Teng, P.K., Riek, R., and Eisenberg, D. (2010). Identifying the amylome, proteins capable of forming amyloid-like fibrils. Proc. Natl. Acad. Sci. USA 107, 3487–3492.

Gosal, W.S., Morten, I.J., Hewitt, E.W., Smith, D.A., Thomson, N.H., and Radford, S.E. (2005). Competing pathways determine fibril morphology in the self-assembly of beta2-microglobulin into amyloid. J. Mol. Biol. 351, 850–864.

Greenwald, J., and Riek, R. (2010). Biology of amyloid: structure, function, and regulation. Structure 18, 1244–1260.

Guo, Y., and Wang, J. (2012). Spectroscopic evidence for polymorphic aggregates formed by amyloid-beta fragments. Chemphyschem 13, 3901–3908.

Han, B., Liu, Y., Ginzinger, S.W., and Wishart, D.S. (2011). SHIFTX2: significantly improved protein chemical shift prediction. J. Biomol. NMR 50, 43–57.

Higurashi, T., Yagi, H., Mizobata, T., and Kawata, Y. (2005). Amyloid-like fibril formation of co-chaperonin GroES: nucleation and extension prefer different degrees of molecular compactness. J. Mol. Biol. 351, 1057–1069.

Hong, J., Jing, Q., and Yao, L. (2013). The protein amide (1)H(N) chemical shift temperature coefficient reflects thermal expansion of the N-H⋯O=C hydrogen bond. J. Biomol. NMR 55, 71–78.

Jain, S., and Udgaonkar, J.B. (2011). Defining the pathway of worm-like amyloid fibril formation by the mouse prion protein by delineation of the productive and unproductive oligomerization reactions. Biochemistry 50, 1153–1161.

Jorgensen, W.L., Chandrasekhar, J., Madura, J.D., Impey, R.W., and Klein, M.L. (1983). Comparison of simple potential functions for simulating liquid water. J. Chem. Phys. 79, 926–935.

Jorgensen, W.L., Maxwell, D.S., and TiradoRives, J. (1996). Development and testing of the OPLS all-atom force field on conformational energetics and properties of organic liquids. J. Am. Chem. Soc. 118, 11225–11236.

Kaminski, G.A., Friesner, R.A., Tirado-Rives, J., and Jorgensen, W.L. (2001). Evaluation and reparametrization of the OPLS-AA force field for proteins via comparison with accurate quantum chemical calculations on peptides. J. Phys. Chem. B 105, 6474–6487.

Kanjee, U., Gutsche, I., Alexopoulos, E., Zhao, B., El Bakkouri, M., Thibault, G., Liu, K., Ramachandran, S., Snider, J., Pai, E.F., et al. (2011). Linkage between the bacterial acid stress and stringent responses: the structure of the inducible lysine decarboxylase. EMBO. J. 30, 931–944.

Knowles, T.P., Vendruscolo, M., and Dobson, C.M. (2014). The amyloid state and its association with protein misfolding diseases. Nat. Rev. Mol. Cell Biol. 15, 384–396.

Korzhnev, D.M., and Kay, L.E. (2008). Probing invisible, low-populated states of protein molecules by relaxation dispersion NMR spectroscopy: an application to protein folding. Acc. Chem. Res. 41, 442–451.

Malet, H., Liu, K., El Bakkouri, M., Chan, S.W., Effantin, G., Bacia, M., Houry, W.A., and Gutsche, I. (2014). Assembly principles of a unique cage formed by hexameric and decameric E. coli proteins. Elife 3, e03653.

Marcoleta, A., Marin, M., Mercado, G., Valpuesta, J.M., Monasterio, O., and Lagos, R. (2013). Microcin e492 amyloid formation is retarded by posttranslational modification. J. Bacteriol. 195, 3995–4004.

Micsonai, A., Wien, F., Kernya, L., Lee, Y.H., Goto, Y., Refregiers, M., and Kardos, J. (2015). Accurate secondary structure prediction and fold recognition for circular dichroism spectroscopy. Proc. Natl. Acad. Sci. USA 112, E3095–E3103.

Miti, T., Mulaj, M., Schmit, J.D., and Muschol, M. (2015). Stable, metastable, and kinetically trapped amyloid aggregate phases. Biomacromolecules 16, 326–335.

Monsellier, E., and Chiti, F. (2007). Prevention of amyloid-like aggregation as a driving force of protein evolution. EMBO Rep. 8, 737–742.

Moran, S.D., and Zanni, M.T. (2014). How to get insight into amyloid structure and formation from infrared spectroscopy. J. Phys. Chem. Lett. 5, 1984–1993.

Neudecker, P., Robustelli, P., Cavalli, A., Walsh, P., Lundstrom, P., Zarrine-Afsar, A., Sharpe, S., Vendruscolo, M., and Kay, L.E. (2012). Structure of an intermediate state in protein folding and aggregation. Science 336, 362–366.

Nilsson, M.R. (2004). Techniques to study amyloid fibril formation in vitro. Methods 34, 151–160.

Pallares, I., Iglesias, V., and Ventura, S. (2015). The Rho termination factor of Clostridium botulinum contains a prion-like domain with a highly amyloidogenic core. Front. Microbiol. 6, 1516.

Palmer, A.G., 3rd, Kroenke, C.D., and Loria, J.P. (2001). Nuclear magnetic resonance methods for quantifying microsecond-to-millisecond motions in biological macromolecules. Methods Enzymol. 339, 204–238.

Pronk, S., Pall, S., Schulz, R., Larsson, P., Bjelkmar, P., Apostolov, R., Shirts, M.R., Smith, J.C., Kasson, P.M., van der Spoel, D., et al. (2013). GROMACS 4.5: a high-throughput and highly parallel open source molecular simulation toolkit. Bioinformatics 29, 845–854.

Sarroukh, R., Goormaghtigh, E., Ruysschaert, J.M., and Raussens, V. (2013). ATR-FTIR: a "rejuvenated" tool to investigate amyloid proteins. Biochim. Biophys. Acta 1828, 2328–2338.

Sattler, M., Schleucher, J., and Griesinger, C. (1999). Heteronuclear multidimensional NMR experiments for the structure determination of proteins in solution employing pulsed field gradients. Prog. Nucl. Magn. Reson. Spectrosc. 34, 93–158.

Shen, Y., Delaglio, F., Cornilescu, G., and Bax, A. (2009). TALOS+: a hybrid method for predicting protein backbone torsion angles from NMR chemical shifts. J. Biomol. NMR 44, 213–223.

Snider, J., Gutsche, I., Lin, M., Baby, S., Cox, B., Butland, G., Greenblatt, J., Emili, A., and Houry, W.A. (2006). Formation of a distinctive complex between the inducible bacterial lysine decarboxylase and a novel AAA+ ATPase. J. Biol. Chem. 281, 1532–1546.

Tollinger, M., Skrynnikov, N.R., Mulder, F.A., Forman-Kay, J.D., and Kay, L.E. (2001). Slow dynamics in folded and unfolded states of an SH3 domain. J. Am. Chem. Soc. 123, 11341–11352.

Torreira, E., Moreno-Del Alamo, M., Fuentes-Perez, M.E., Fernandez, C., Martin-Benito, J., Moreno-Herrero, F., Giraldo, R., and Llorca, O. (2015). Amyloidogenesis of bacterial prionoid RepA-WH1 recapitulates dimer to monomer transitions of RepA in DNA replication initiation. Structure 23, 183–189.

Toyama, B.H., and Weissman, J.S. (2011). Amyloid structure: conformational diversity and consequences. Annu. Rev. Biochem. 80, 557–585.

Tsolis, A.C., Papandreou, N.C., Iconomidou, V.A., and Hamodrakas, S.J. (2013). A consensus method for the prediction of 'aggregation-prone' peptides in globular proteins. PLoS One 8, e54175.

vandenAkker, C.C., Engel, M.F., Velikov, K.P., Bonn, M., and Koenderink, G.H. (2011). Morphology and persistence length of amyloid fibrils are correlated to peptide molecular structure. J. Am. Chem. Soc. 133, 18030–18033.

Walsh, P., Simonetti, K., and Sharpe, S. (2009). Core structure of amyloid fibrils formed by residues 106-126 of the human prion protein. Structure 17, 417–426.

Walsh, I., Seno, F., Tosatto, S.C., and Trovato, A. (2014). PASTA 2.0: an improved server for protein aggregation prediction. Nucleic Acids Res. 42, W301–W307.

Wishart, D., and Sykes, B. (1994). The $^{13}$C chemical-shift index: a simple method for the identification of protein secondary structure using $^{13}$C chemical-shift data. J. Biomol. NMR 4, 171–180.

Wishart, D.S., Bigam, C.G., Holm, A., Hodges, R.S., and Sykes, B.D. (1995). $^{1}$H, $^{13}$C and $^{15}$N random coil NMR chemical shifts of the common amino acids. I. Investigations of nearest-neighbor effects. J. Biomol. NMR 5, 67–81.

Wong, K.S., Snider, J.D., Graham, C., Greenblatt, J.F., Emili, A., Babu, M., and Houry, W.A. (2014). The MoxR ATPase RavA and its cofactor ViaA interact with the NADH:ubiquinone oxidoreductase I in Escherichia coli. PLoS One 9, e85529.

Zou, Y., Li, Y., Hao, W., Hu, X., and Ma, G. (2013). Parallel beta-sheet fibril and antiparallel beta-sheet oligomer: new insights into amyloid formation of hen egg white lysozyme under heat and acidic condition from FTIR spectroscopy. J. Phys. Chem. B 117, 4003–4013.